Available online at www.sciencedirect.com
ScienceDirect
International Journal of Heat and Mass Transfer 50 (2007) 4724–4735
International Journal of HEAT and MASS TRANSFER
www.elsevier.com/locate/ijhmt

Large eddy simulations of the flow field and temperature separation in the Ranque–Hilsch vortex tube

Tanvir Farouk, Bakhtier Farouk *

Department of Mechanical Engineering and Mechanics, Drexel University, Philadelphia, PA 19104, United States

Received 22 October 2006; received in revised form 5 March 2007
Available online 27 June 2007

Abstract

A computational fluid dynamic model is used to predict the flow fields and the associated temperature separation within a Ranque–Hilsch vortex tube. The large eddy simulation (LES) technique was employed for predicting the flow and temperature fields in the vortex tube. A vortex tube with a circumferential inlet stream and an axial (cold) outlet stream and a circumferential (hot) outlet stream was considered. The temporal evolutions of the axial, radial and azimuthal components of the velocity along with the temperature, pressure and density fields within the vortex tube are simulated. Performance curves (temperature separation versus cold outlet mass fraction) were obtained for a specific vortex tube with a given inlet mass flow rate. Simulations were carried out for varying amounts of cold outlet mass flow rates. Predictions from the present large eddy simulations compare favorably with available experimental measurements.

Keywords: Ranque–Hilsch vortex tube; Modeling; Large eddy simulations; Temperature separation

1. Introduction

The vortex tube is a simple device with no moving parts that is capable of dividing a high pressure flow into two relatively lower pressure flows with temperatures higher and lower than that of the incoming flow. The device consists of a simple circular tube, with one or more azimuthal nozzles for flow inlet and two outlets for flow exits. High pressure air enters the tube azimuthally at one end and produces a strong vortex flow in the tube. The gas is separated into two streams having different temperatures, one flowing along the outer wall and the other along the axis of the tube. The gas streams leaving through the exits located along the outer wall and along the axis are at higher and lower temperatures, respectively, than the inlet gas temperature. This effect is referred to as the "temperature separation" and was first observed by Ranque in 1931 when he was studying processes in a dust separation cyclone [1]. Intense experimental and numerical studies of the Ranque–Hilsch vortex tubes began since then and continue even today [2–9]. Despite the simplicity of its geometry, the energy separation phenomenon is quite intriguing. Various theories have been proposed in the literature to explain the "temperature separation" effect since the initial observations by Ranque [1]. In his pioneering work on the vortex tube, Hilsch [10] suggested that angular velocity gradients in the radial direction give rise to frictional coupling between different layers of the rotating flow resulting in the migration of energy via shear work from the inner layers to the outer layers. Other investigators have attributed the energy separation to work transfer via compression and expansion. Several variations of this theory are described in the literature, differing according to the mechanism that drives the fluid motion. Harnett and Eckert [11] invoked turbulent eddies, Ahlborn and Gordon [12] described an embedded secondary circulation and Stephan et al. [13] proposed the formation of Görtler vortices on the inside wall of the vortex tube that drive the fluid motion. All these theories treat individual particles as small refrigeration systems, each undergoing thermodynamic cycles that are

* Corresponding author.
E-mail address: bfarouk@coe.drexel.edu (B. Farouk).

0017-9310/$ - see front matter © 2007 Elsevier Ltd. All rights reserved.
doi:10.1016/j.ijheatmasstransfer.2007.03.048

Nomenclature

c_p	specific heat at constant pressure (J/kg K)
C_s	Smagorinsky constant
H	total enthalpy (kJ/kg)
k	thermal conductivity (W/m K)
m	mass flow rate (m s^{-1})
p	pressure (Pa)
R	universal gas constant (J/mol K)
S	strain rate
t	time (s)
T	temperature (K)
$\boldsymbol{u}$	velocity vector (m s^{-1})
u_x	velocity component in the x direction
u_r	velocity component in the r direction
u_θ	velocity component in the θ direction

Greek symbols

ΔT_{hc}	temperature difference between hot and cold ends
v_t	eddy viscosity (kg/m s)
ρ	density (kg/m^3)
τ	shear stress (N/m^2)
τ_{ij}	stress tensor component

Subscripts

c	cold gas
h	hot gas
r	radial direction
x	axial direction
θ	azimuthal direction

powered by energy from the flow itself. Kurosaka [14] reported the "temperature separation" to be a result of acoustic streaming effect that transfer energy from the cold core to the hot outer annulus. Gutsol [15] hypothesized the energy separation to be a consequence of the interaction of micro volumes in the vortex tube. Despite all the proposed theories, none has been able to explain the "temperature separation" effect satisfactorily.

Recent efforts have utilized modeling to explain the fundamental principles behind the energy separation produced by the vortex tube. Ahlborn et al. [4] showed the dependence of vortex tube performance on normalized pressure drop with a numerical model. Frohlingsdorf and Unger [6] used a fluid dynamics model that included the compressible and turbulent effects. Their numerical predictions qualitatively matched the experimental results of Bruun [2]. Aljuwayhel et al. [8] utilized a fluid dynamics model of the vortex tube to understand the process that drive the power separation phenomena. They report that the energy separation exhibited by the vortex tube is due to the work transfer caused by a torque produced by viscous shear acting on a rotating control surface that separates the cold flow region and the hot flow region. Skye et al. [9] used a model similar to that of Aljuwayhel et al. [8]. They also measured the inlet and outlet temperatures of the vortex tube and compared with the predictions from the fluid dynamics model. The temperature separation predicted by their model for a commercially available vortex tube was found to be in reasonable agreement to the experimental measurements. Behera et al. [7] conducted both numerical and experimental studies towards the optimization of the Ranque–Hilsch vortex tube. Their numerical study resulted in obtaining the optimum parameters (cold end diameter, length to diameter ratio) for the maximum temperature separation. All of these models used the compressible form of the Navier–Stokes equation, and the turbulence effects were included using either the standard k–ε or the renormalization group (RNG) k–ε model.

In the present study, a compressible form of the Navier–Stokes equation together with the large eddy simulation (LES) technique has been used to simulate the phenomenon of flow pattern and temperature separation in a Ranque–Hilsch vortex tube with a circumferential inlet port, and a cold axial and a hot circumferential outlet ports (as shown in Fig. 1). This arrangement is a bit different from the geometry used by Aljuwayhel et al. [8] where the flow enters the tube from the top surface with axial and angular components of velocities rather than the circumferential outer wall (as considered in the present study) with radial and angular components of velocities.

The Reynolds averaged Navier–Stokes simulations (RANS) method attempts to model the turbulence by performing time or space averaging. The averaging process wipes out most of the important characteristics of a time-dependent solution. The direct numerical simulation (DNS) technique on the other hand attempts to solve all time and spatial scales in the velocity field. As a result, the solution is accurate but numerically very intensive. LES is considered somewhere in between DNS and RANS with respect to both physical resolution and computational costs. LES inherits the universality of DNS, allowing accurate prediction of the coherent structures in turbulent flows. The computational cost for LES is lower than that for DNS because the resolution requirements for LES are of the same order as those for RANS.

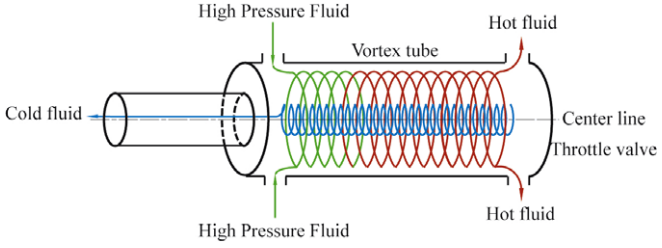

Fig. 1. Schematic diagram of the Ranque–Hilsch vortex tube with simplified representation of the flowlines for the hot and cold gas.

LES of the vortex tube flows have not been reported in the literature. The main objective of this work is to apply the LES technique in predicting the flow field and temperature separation in a vortex tube. With the chosen geometry, an axisymmetric formulation is used for the prediction of the velocity and temperature fields in the vortex tube. For a given inlet flow rate, the exit pressure at the hot exit port is varied to study the 'temperature separation effect' between the two outlet streams.

2. Schematic of the problem geometry

Fig. 2 depicts the computational domain for the vortex tube geometry considered in this study. An axisymmetric flow field is considered where a circumferential inlet and a circumferential outlet (for the hot stream) are considered. This simplification results in considerable reduction in the computing time for the LES predictions, while preserving the three-dimensional features of the flow field. In addition, due to the radial symmetry only one-half of the geometry is considered as the computational domain.

The computational domain used for the simulations (Fig. 2) is similar to that of the past study of Skye et al. [9]. The length and the radius of the vortex tube are set to 100 mm and 10 mm, respectively. The tube length of the cold gas exit is set to 25 mm. The line a–h is the axis of symmetry. The boundary d–e is the gas flow inlet having a dimension of 3 mm. The boundary f–g located at the right most end of the vortex tube is the hot gas outlet having a width of 1.5 mm. The boundary a–b is the cold gas outlet having a radius of 3 mm.

The inlet pressure and the cold exit pressure were fixed at 400 kPa and 101 kPa, respectively, for all the simulations. The velocity at the inlet high pressure flow consists of a radial component of 20 m s^{-1} and an azimuthal component of 200 m s^{-1}. The only parameter varied during the simulations in this study was the hot gas outlet pressure. This results in the variation of mass flow rates in the cold and the hot exit streams. The variable and fixed parameters for the numerical study are listed in Table 1. Details of the mathematical model and the boundary conditions considered for the simulations are discussed in the following section.

3. Mathematical model

The compressible turbulent flows in the vortex tube are governed by the conservation of mass, momentum and energy equations. The mass, momentum and the energy conservation and the state equation solved are as follows:

$$\frac{\partial \rho}{\partial t} + \nabla \cdot (\rho \mathbf{u}) = 0 \tag{1}$$

$$\frac{\partial (\rho \mathbf{u})}{\partial t} + \nabla \cdot (\rho \mathbf{u}\mathbf{u}) = -\nabla p + \nabla \cdot (\tau) \tag{2}$$

$$\frac{\partial (\rho H)}{\partial t} + \nabla \cdot (\rho v H) = \frac{\partial p}{\partial t} + \nabla \left(\frac{k}{c_p} \nabla H \right) - \nabla \cdot (\tau \cdot \mathbf{u}) \tag{3}$$

$$p = \rho R T \tag{4}$$

where ρ is the density of the fluid, $\mathbf{u}$ is the fluid velocity, p is the static pressure, τ is the viscous stress tensor, H is the total enthalpy, k and c_p are the thermal conductivity and spe-

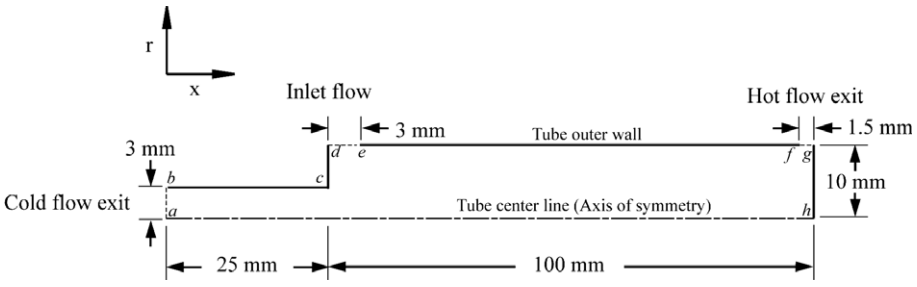

Fig. 2. Schematic of the computational domain.

Table 1
Variable and fixed parameters for the vortex tube simulations

Case	Variable parameter		Fixed parameters		
	Hot exit pressure (kPa)	Cold exit pressure (kPa)	Inlet radial velocity U_r (m s^{-1})	Inlet azimuthal velocity U_θ (m s^{-1})	Inlet pressure (kPa)
1	105	101.32	−20.00	200.00	400.00
2	60				
3	70				
4	80				
5	90				
6	100				
7	110				
8	115				

cific heat of the fluid, respectively, R is the ideal gas constant and T is the gas temperature.

The total temperature, T_{total} is expressed in the following expression:

$$T_{\text{total}} = T + \frac{1}{2c_{\text{p}}}(u_x^2 + u_r^2 + u_\theta^2) \tag{5}$$

where, T is the static gas temperature, c_p is the specific heat and u_x, u_r, and u_θ the velocity component in the x, r, and θ directions.

3.1. Turbulence model

The LES technique is used to take into account the effect of turbulence in the vortex tube flow. The application of the LES techniques is aimed towards extracting greater temporal and spatial fidelity. In the LES technique, small scale turbulence is filtered out from the Navier–Stokes equation, and a model is used to evaluate the small scales. The small scales are computed from a turbulence model known as the sub-grid scale model. The sub-grid scale stress model used in the present calculation is the Smagorinsky model [16]. According to the Smagorinsky model the sub-grid scale Reynolds stress tensor is given by:

$$\tau_{ij} = \nu_t\left(\frac{\partial u_i}{\partial x_j} + \frac{\partial u_j}{\partial x_i} - \frac{2}{3}\frac{\partial u_k}{\partial x_k}\right) \tag{6}$$

where ν_t is the eddy viscosity.

The eddy viscosity is expressed in the following way:

$$\nu_t = (C_{\text{s}}\Delta)^2|\overline{S}| \tag{7}$$

where C_{s} (=0.1) is the Smagorinsky constant, Δ is the filter width (=0.06×10^{-3} m) and $\overline{S}$ is the local strain rate which is expressed in the following way:

$$|\overline{S}| = \sqrt{2\left(\frac{\partial u_x}{\partial x}\right)^2 + 2\left(\frac{\partial u_r}{\partial r}\right)^2 + 2\left(\frac{\partial u_\theta}{r\partial\theta}\right)^2 + \left(\frac{\partial u_r}{\partial r} + \frac{\partial u_x}{\partial x}\right)^2 + \left(\frac{\partial u_\theta}{r\partial\theta} + \frac{\partial u_x}{\partial x}\right)^2 + \left(\frac{\partial u_\theta}{r\partial\theta} + \frac{\partial u_r}{\partial r}\right)^2} \tag{8}$$

The resulting filtered Navier–Stokes equations are solved for the large scale motion which is responsible for most of the momentum and energy transport.

3.2. Boundary conditions

The boundary conditions provided at the different regions to simulate the vortex tube phenomena are as follows:

- A radial velocity of -20 m s^{-1} and an azimuthal velocity of 200 m s^{-1} was provided at the inlet. The total temperature at the inlet was set to 300 K. The pressure at the inlet was set to 400 kPa. The values for the inlet pressure and temperature are similar to the experimental data of Skye et al. [9]. The inlet velocities were chosen to match the experimental inlet mass flow rate of Skye et al. [9].
- Atmospheric pressure was specified at the cold exit of the vortex tube. Zero gradient boundary condition for the temperature was used.
- The pressure boundary condition at the hot exit was varied in order to control the mass flow rates among the two exits. The temperature at the hot exit was assigned a zero gradient boundary condition.
- The tube walls were considered to be adiabatic with no slip boundary condition for the velocity components.

3.3. Numerical model

The CFD-ACE+ code [17] was used for the large eddy simulations reported in this paper. The numerical scheme for solving the governing equations is based on the finite volume approach. For the convective–diffusive terms in the mass, momentum and energy conservation equations a second order upwind scheme [18] is used. A Crank–Nicolson scheme is used for the time derivatives in the continuity, momentum and energy equations. The Kolmogorov time scale calculated from the micro scale relations was found to be 2×10^{-4} s. A 10 μs time-step size was chosen for the Crank–Nicolson scheme, which is smaller than the Kolmogorov time scale. Details about the spatial grid distribution are discussed in the next section. The implicit calculations within a given time-step are continued until the variation in the variables is within 10^{-05}% of the value of the variable from the previous iteration. The time marching calculations were terminated when a pseudo steady-state behavior was observed.

4. Results and discussion

Simulations were carried out for the vortex tube for eight different cases with varying hot end pressure values. The operating parameters for the cases studied are listed in Table 1. To achieve grid independent solutions, simulations were carried out for different grid sizes for the base case (Case 1). Simulations were carried out for four different grid sizes 300×80 (240,00 cells), 400×120 (480,00 cells), 500×160 (80,000 cells) and 550×180 (99,000 cells). In all cases, a time-step of 10 μs was used. Following Behera et al. [7], the total temperature difference was considered to be the key parameter for the grid-independence study. The total temperature difference is defined as the dif-

ference between the spatially and temporally averaged total temperatures at the hot and cold exit ($\Delta T_{\text{total,hc}} = \overline{T}_{\text{total,h}} - \overline{T}_{\text{total,c}}$) where, $\overline{T}_{\text{total}}$ is the time averaged total temperature defined as $\overline{T}_{\text{total}} = \frac{1}{\tau}\int_{t=t_0}^{t=t_0+\tau} T_{\text{total}}\,\mathrm{d}t$, averaged over the exit areas. The time averaging was performed between 0.5 and 1.0 s with 50,000 time-steps. For Case 1 the hot exit pressure was set to 105 kPa. Increasing the number of cells beyond 80000 (500 × 160 grid size) does not result in significant increase in the accuracy (Fig. 3). All the results reported in this paper are thus for a grid size of 500 × 160 (80,000 cells).

The LES scheme was able to capture the inherent velocity fluctuations in the flow field. Temporal variation of the axial velocity, u_x for Case 1 at the axial and radial locations of 75 mm and 5 mm, respectively, are shown in Fig. 4. The period of time shown is between 0 and 1 s. The root mean square (rms) value for the axial velocity was found to be 12.373 m s^{-1}. After 0.2 s, the system was found to reach a quasi-steady state condition. The initial large fluctuation diminishes but steady fluctuations are still observed. Fig. 5 shows the corresponding temporal variation of the radial velocity u_r component (Case 1) at the axial and radial locations of 75 mm and 5 mm. The rms value of the radial velocity was found to be 0.997 m s^{-1}. Similar to the axial

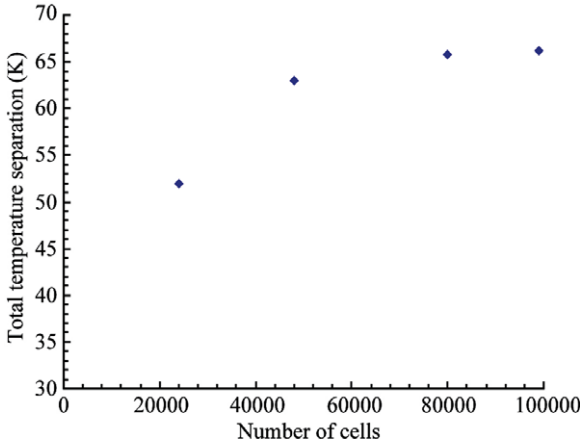

Fig. 3. Grid size dependence study on total temperature separation (Case 1).

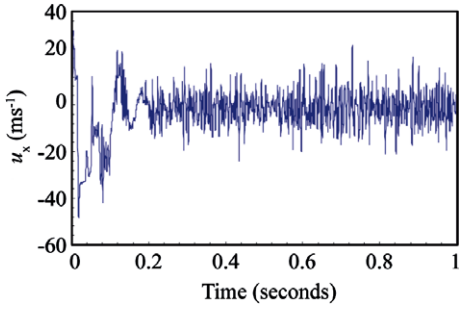

Fig. 4. Temporal variation of axial velocity, u_x at a given location within the vortex tube ($x = 75$ mm, $r = 5$ mm) (Case 1).

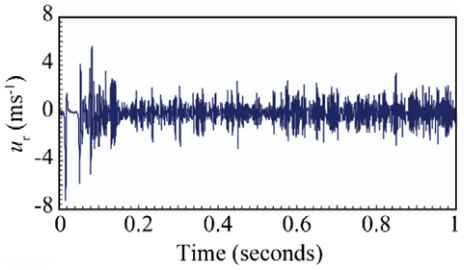

Fig. 5. Temporal variation of radial velocity, u_r at a given location within the vortex tube ($x = 75$ mm, $r = 5$ mm) (Case 1).

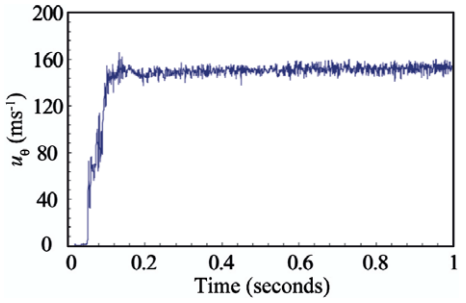

Fig. 6. Temporal variation of azimuthal velocity, u_θ at a given location within the vortex tube ($x = 75$ mm, $r = 5$ mm) (Case 1).

velocity temporal variations, the fluctuations become steady after 0.2 s. During the quasi-steady state the radial velocity was observed to fluctuate between ±1.75 m s^{-1}. Fig. 6 depicts the variation of the azimuthal velocity component u_θ (Case 1) at the above location as a function of time. As observed for the axial and radial velocity components, the azimuthal velocity component was also observed to reach a quasi-steady state after about 0.2 s. The rms value of the azimuthal velocity was found to be 144.273 m s^{-1}. The temporal variation of the temperature, pressure and density (not reported here) also showed similar quasi-steady behavior after about 0. 2 s.

Fig. 7 shows the time averaged radial profiles of the axial velocity $\bar{u}_x$ at different axial locations ($x = 50$ mm, $x = 75$ mm and $x = 100$ mm) for Case 1. The time averaged axial component of velocity $\bar{u}_x$ is given as, $\bar{u}_x = \frac{1}{\tau}\int_{t=t_0}^{t=t_0+\tau} u_x\,\mathrm{d}t$ where $t_0 = 0.5$ s and $\tau = 0.5$ s also. The maximum axial velocity is near the tube wall and the direction of the flow near the wall is towards the hot end exit and the direction of the flow along the axis is towards the cold end exit. It was observed that the maximum value of the axial velocity decreased with increasing axial distance. At axial locations of 50, 75 and 100 mm the maximum axial velocity was found to be 78 m s^{-1}, 71 m s^{-1} and 61 m s^{-1}, respectively. The axial velocity profiles show that the flow reversal takes place at about 7 mm from the center of the tube. The axial velocity in the cold core is directed towards the cold end exit. The axial velocity in the cold core was found to increase with a decrease in the axial distance.

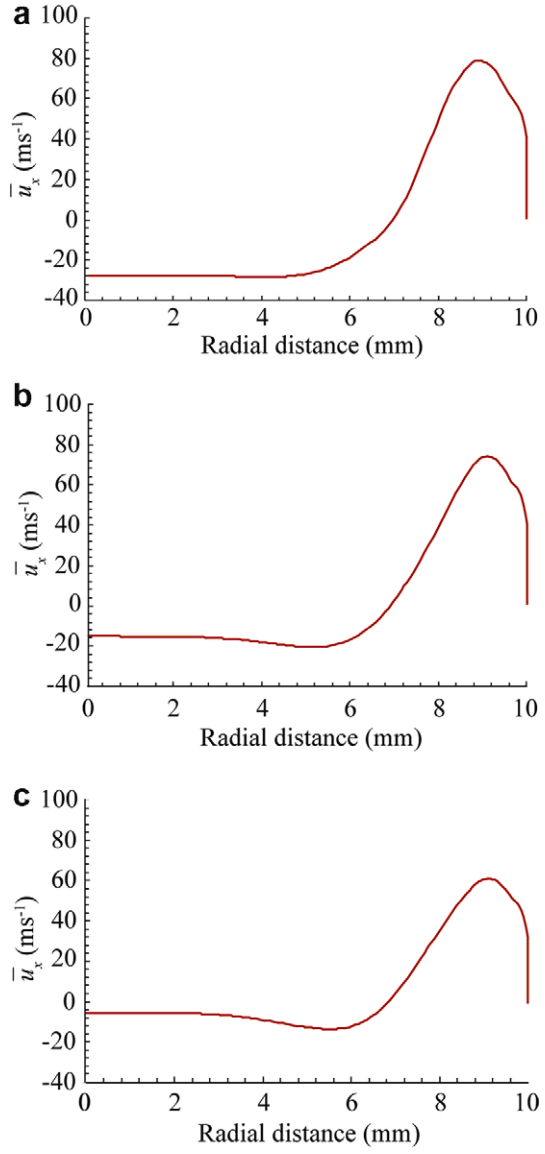

Fig. 7. Radial profiles of time averaged axial velocity, $\bar{u}_x = \frac{1}{\tau}\int_{t=t_0}^{t=t_0+\tau} u_x \, dt$ at: (a) $x = 50$ mm, (b) $x = 75$ mm and (c) $x = 100$ mm (Case 1). Time average was performed between 0.5 and 1.0 s.

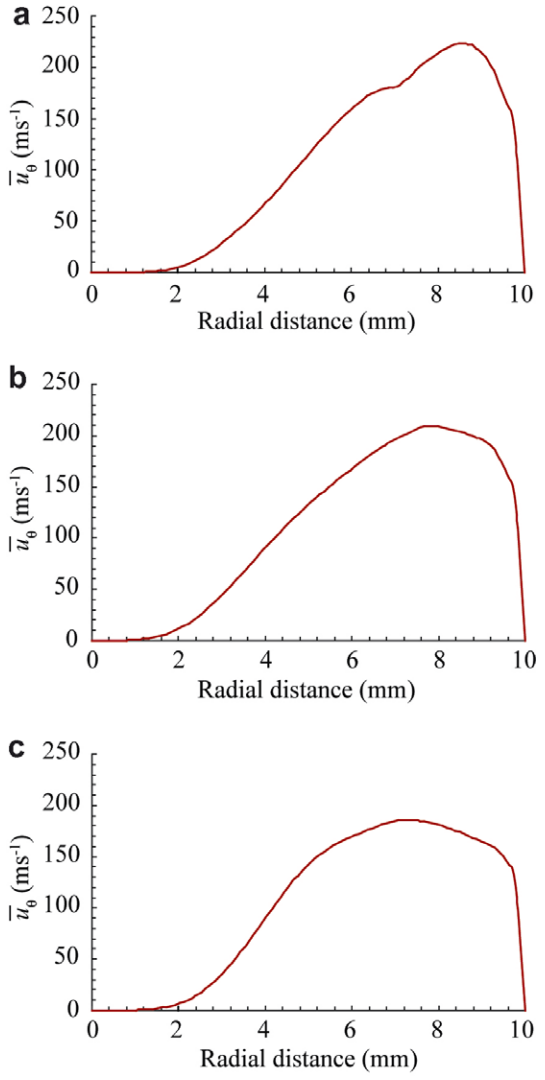

Fig. 8. Radial profiles of time averaged azimuthal velocity, $\bar{u}_\theta = \frac{1}{\tau}\int_{t=t_0}^{t=t_0+\tau} u_\theta \, dt$ at: (a) $x = 50$ mm, (b) $x = 75$ mm and (c) $x = 100$ mm (Case 1). Time average was performed between 0.5 and 1.0 s.

Fig. 8 depicts the radial profiles for the time averaged azimuthal velocity $\bar{u}_\theta$ at different axial locations ($x = 50$ mm, $x = 75$ mm and $x = 100$ mm) for Case 1. Comparing the velocity components, it is observed that the azimuthal velocity has the highest value. The azimuthal velocity has twice the magnitude of the axial velocity. The magnitude of the azimuthal velocity decreases towards the hot end exit. The radial profile of the azimuthal velocity indicates a free vortex near the wall and the values become negligibly small at the core. Our results thus do not show a forced vortex near the axis of the tube as claimed by Gutsol [15] and Behera et al. [7]. It is noted that there is no change in the direction of rotation of the flow field in the entire domain.

The time averaged values of the radial velocity component $\bar{u}_r$ (Fig. 9) is significantly low in magnitude compared to the axial and the azimuthal components. The radial velocity component was found to be positive near the tube wall but it was mostly negative along the tube radius. This indicates possibilities of energy transfer in the radial plane. The radial velocity was also observed to decrease with increasing axial distance away from the entrance. The time averaged axial and radial (but not the azimuthal) velocity profiles obtained at different axial locations of the vortex tube are in good conformity with those observed by Gutsol [15] and Behera et al. [7] albeit for different geometries of the vortex tube.

Fig. 10 shows the instantaneous streamlines in the r–x plane for Case 1 at 0.6 s. The streamlines were calculated from the instantaneous radial u_r and axial u_x velocity components. It can be seen that there exists a reversal of the flow in the inner region of the tube. Vortex structures are observed through out the tube. Small vortices were observed mostly in the cold (central) region of the tube.

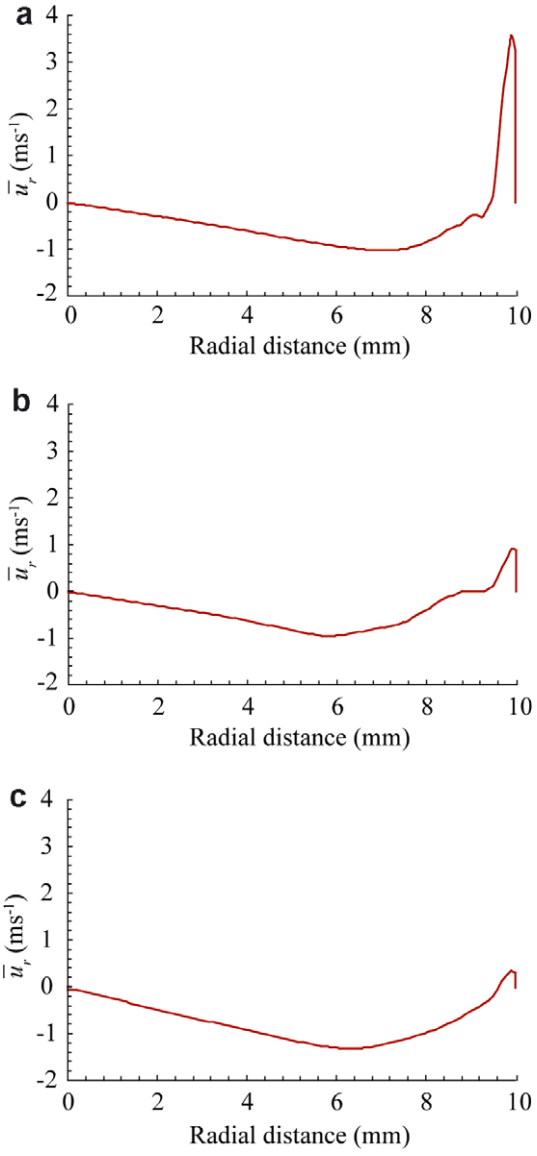

Fig. 9. Radial profiles of time averaged radial velocity, $\bar{u}_r = \frac{1}{\tau}\int_{t=t_0}^{t=t_0+\tau} u_r \, dt$ at: (a) $x = 50$ mm, (b) $x = 75$ mm and (c) $x = 100$ mm (Case 1). Time average was performed between 0.5 and 1.0 s.

These vortices were not observed by Aljuwayhel et al. [8] and Behera et al. [7]. For Case 1, the time averaged streamlines in the r–x plane for the entire vortex tube were also obtained. The streamlines were calculated from the time averaged radial $\bar{u}_r$, and axial $\bar{u}_x$ velocity components. The time averaging was performed between 0.5 s and 1.0 s. The resulting time averaged streamlines are depicted in Fig. 11. The time averaged flow inside the vortex tube in the r–x plane has an outer peripheral flow, and an inner core flow. The outer peripheral flow happens to occur over a small region where as the inner core flow is observed to occur in the bulk of the tube. The peripheral flow leaving through the hot exit is seen for the fluids entering through the lower part of the inlet (near point 'e' in Fig. 2). A small secondary circulation was seen to form near the cold end exit. The secondary circulation is a performance degrading mechanism in vortex tubes [7]. The secondary circulation will result in enhanced mixing and increase in the cold exit temperature. The cold end diameter can be optimized to prevent the secondary circulation from occurring. A secondary circulation near the cold exit was observed by Aljuwayhel et al. [8]. Behera et al. [7] also had shown the presence of secondary circulation near the cold exit for the case of non-optimally chosen cold end diameter.

The instantaneous contours for the azimuthal velocity, u_θ at time 0.6 s is shown in Fig. 12 for Case 1. The azimuthal velocity has the maximum magnitude near the nozzle inlet. The magnitude is found to decrease with an increase in the axial distance. The azimuthal velocity has the minimum magnitude near the hot gas exit. Along the radial direction of the tube, the azimuthal velocity is observed to have the minimum magnitude near the tube axis. Small fluctuations near the tube wall are observed. Time integration was done to obtain the time averaged azimuthal velocity $\bar{u}_\theta = \frac{1}{\tau}\int_{t=t_0}^{t=t_0+\tau} u_\theta \, dt$. The resulting time averaged azimuthal velocity contours are shown in Fig. 13. The time averaging smoothes out the small fluctuations observed in the instantaneous velocity contours (Fig. 12). Throughout the vortex tube, the inner core is observed to have negligible azimuthal velocity values.

From the computed time-dependent velocity fields, particle traces (path lines) for two specific fluid elements that exit the flow field via the cold and hot exits, respectively, are shown in Figs. 14 and 15, respectively. The fluid element that leaves by the cold exit advances towards the end of the vortex tube with a swirling motion (Fig. 14). The flow direction however reverses near the tube end and the particle starts moving towards the cold exit, without reversing the direction of rotation. As the particle starts moving towards the cold exit, the swirling motion was found to decrease. Fig. 15 depicts the particle trace (path line) of a fluid element that exits via the hot exit. After

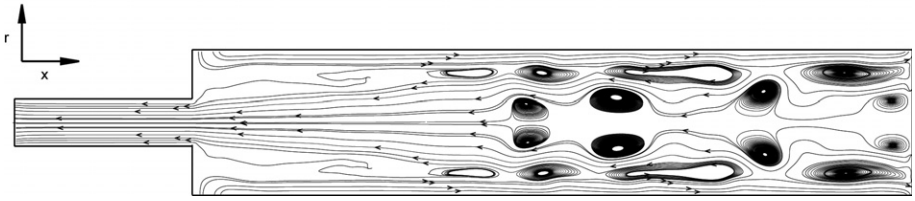

Fig. 10. Instantaneous streamlines for the vortex tube in r–x plane at 0.6 s (Case 1).

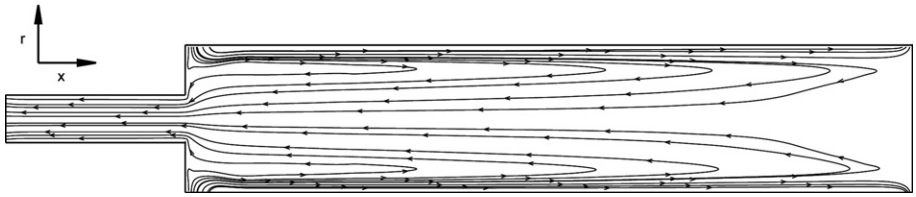

Fig. 11. Time averaged streamlines for the vortex tube in r–x plane. Time averaging was performed between 0.5 and 1.0 s (Case 1).

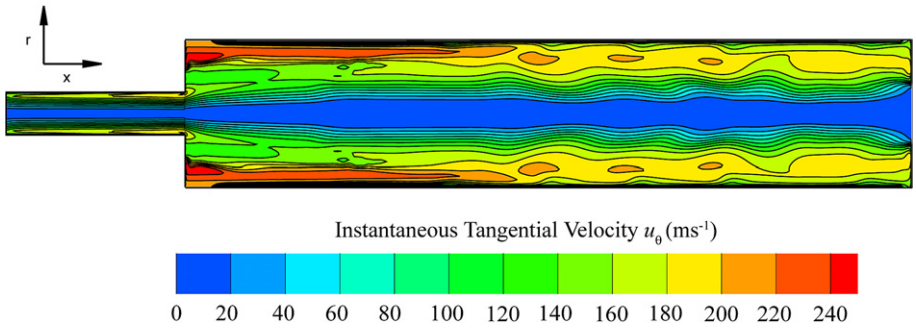

Fig. 12. Instantaneous azimuthal velocity, u_θ contours for the entire vortex tube in the r–x plane at 0.6 s (Case 1).

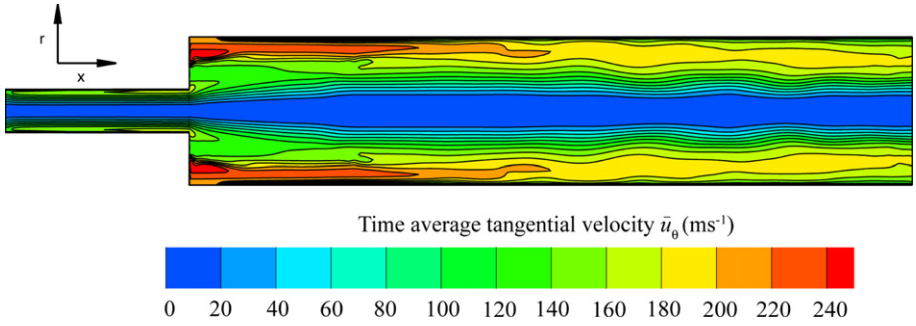

Fig. 13. Time averaged azimuthal velocity, $\bar{u}_\theta = \frac{1}{\tau}\int_{t=t_0}^{t=t_0+\tau} u_\theta \, dt$ contours for the entire vortex tube in the r–x plane. Time average was performed between 0.5 and 1.0 s (Case 1).

entering the tube the particle advances towards the hot exit with a swirling motion.

Contour plots of the time averaged total temperature ($\overline{T}_{\text{total}} = \frac{1}{\tau}\int_{t=t_0}^{t=t_0+\tau} T_{\text{total}} \, dt$) in the r–x plane is shown in Fig. 16 (Case 1). The time averaging was performed in between 0.5 s and 1.0 s with 50,000 time-steps. The peripheral flow is warm and the core flow is cold relative to the inlet temperature. For a cold gas fraction of 0.65 (Case 1) a hot gas total temperature of 350 K and a cold gas total temperature of 260 K were predicted where the inlet gas total temperature was 300 K. Time averaged radial profiles of the total temperature $\overline{T}_{\text{total}}$ at different axial locations ($x = 50$ mm, $x = 75$ mm and $x = 100$ mm) for Case 1 are presented in Fig. 17. At an axial distance of 50 mm, the maximum and the minimum total temperatures were found to be 320 K and 270 K, respectively. The cold region was found to exist up to a radial distance of 4.5 mm from the tube center. The maximum total temperature was observed to exist near the periphery of the tube wall. At the tube wall the total temperature is found to decrease, this is due to the no slip boundary condition at the tube wall. For an axial location of 75 mm, the maximum and minimum total temperatures were found to be 325 K and 274 K, respectively. A maximum total temperature of 329 K and a minimum total temperature of 276 K were observed at an axial location of 100 mm. Time averaged radial profiles of the static temperature $\overline{T}_{\text{static}}$ at different axial locations ($x = 50$ mm, $x = 75$ mm and $x = 100$ mm) for Case 1 are presented in Fig. 18. The static temperature variation is essentially similar to that of the total temperature albeit the static temperature values are lower than the total values near the outer periphery of the vortex tube. The predicted temperature profiles are a result of the kinetic energy distribution in the vortex tube. The fluid at the core of the vortex tube has very low kinetic energy due to the minimum azimuthal fluid velocity at the central zone of the tube. From the azimuthal velocity profiles (Fig. 8), it was observed that the azimuthal velocity had almost negligible value at the core of the vortex tube. The azimuthal velocity being the major component, the kinetic energy at the inner core thus also

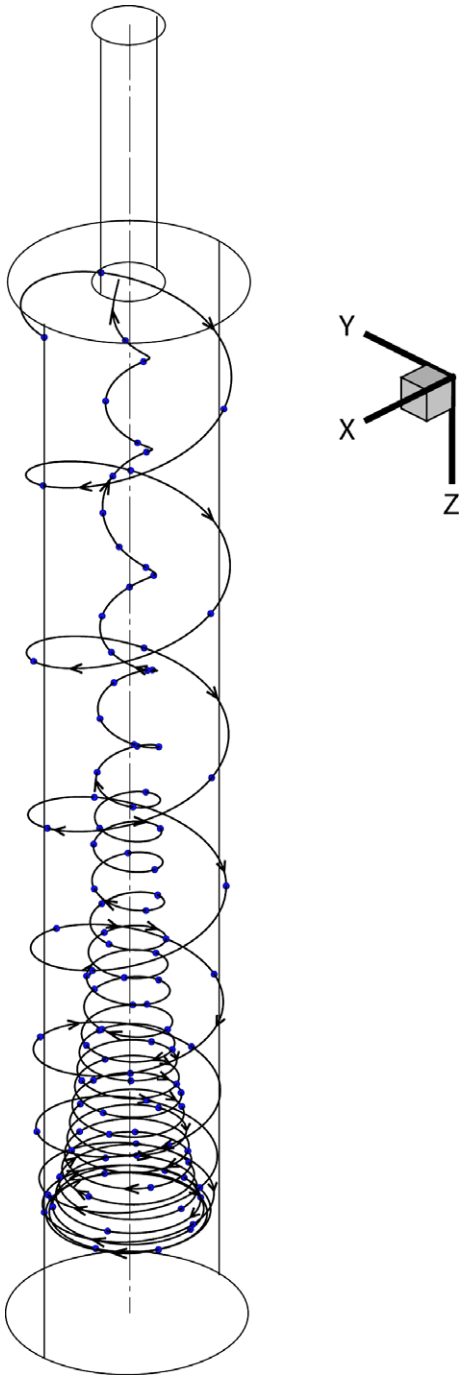

Fig. 14. Stream trace for the inner core fluid flow in the entire vortex tube in three-dimensional space (Case 1).

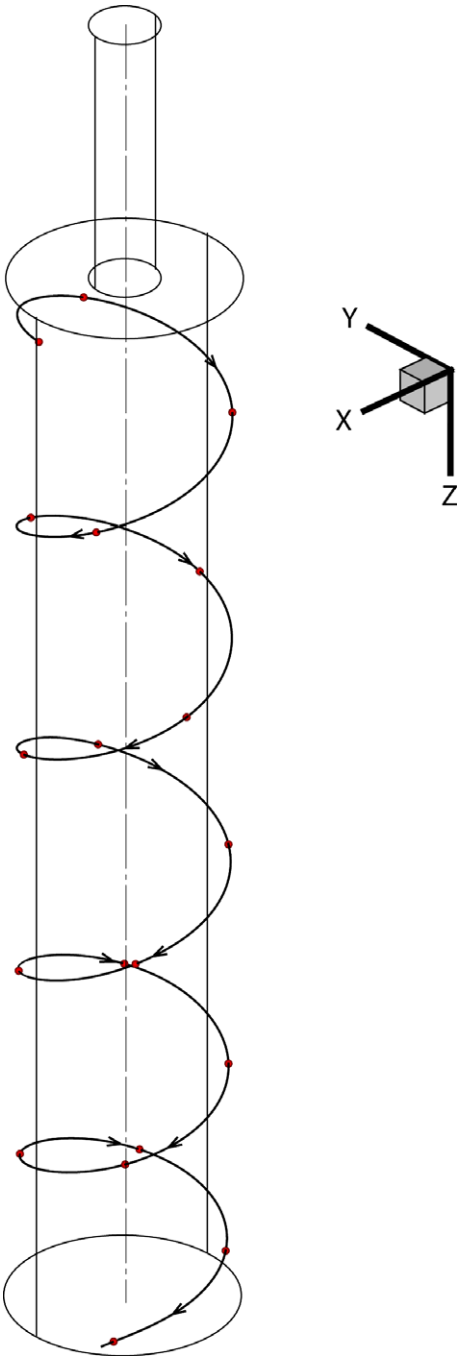

Fig. 15. Stream trace for the outer peripheral fluid flow in the entire vortex tube in three-dimensional space (Case 1).

has low values. Comparing the total temperature and the azimuthal velocity profiles (Figs. 17 and 8), the low temperature zone (about 2 mm near the axis) in the core coincides with the negligible azimuthal velocity zone. The static temperature profiles (Fig. 18) obtained thereby shows an increase of the temperature values towards the periphery.

A parametric study was carried out to investigate the effect of varying the mass flow rates at the cold and hot exits on the temperature separation. This was achieved by varying the outlet pressure at the hot exit systematically (see Table 1). Following Skye et al. [9], the total temperature separation at the cold and hot exits is the absolute difference between the inlet temperature and the respective exit temperatures. For the hot exit temperature separation, $|\overline{T}_{in} - \overline{T}_{out,h}|$ (Fig. 19a) it was found that the temperature separation increased with an increase in the cold mass fraction. The time averaged total temperatures at the hot and cold ends were spatially averaged to obtain the values plotted. A maximum hot temperature separation of 62.3 K was observed for a cold mass fraction of 0.78. Fig. 19b shows similar results for the cold exit where

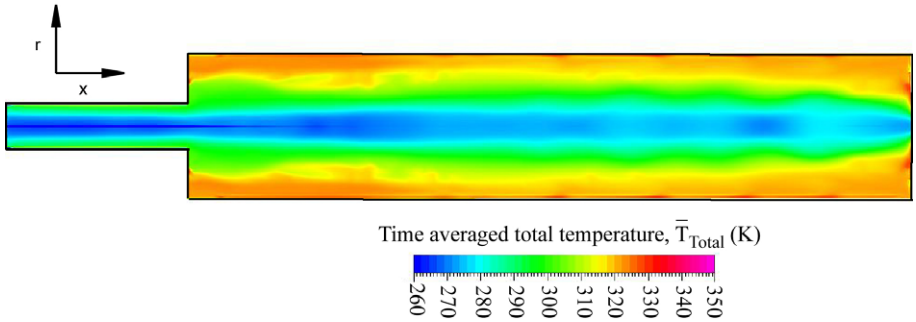

Fig. 16. Time averaged total temperature contours for the vortex tube in the r–x plane (Case 1). Time average was performed between 0.5 and 1.0 s.

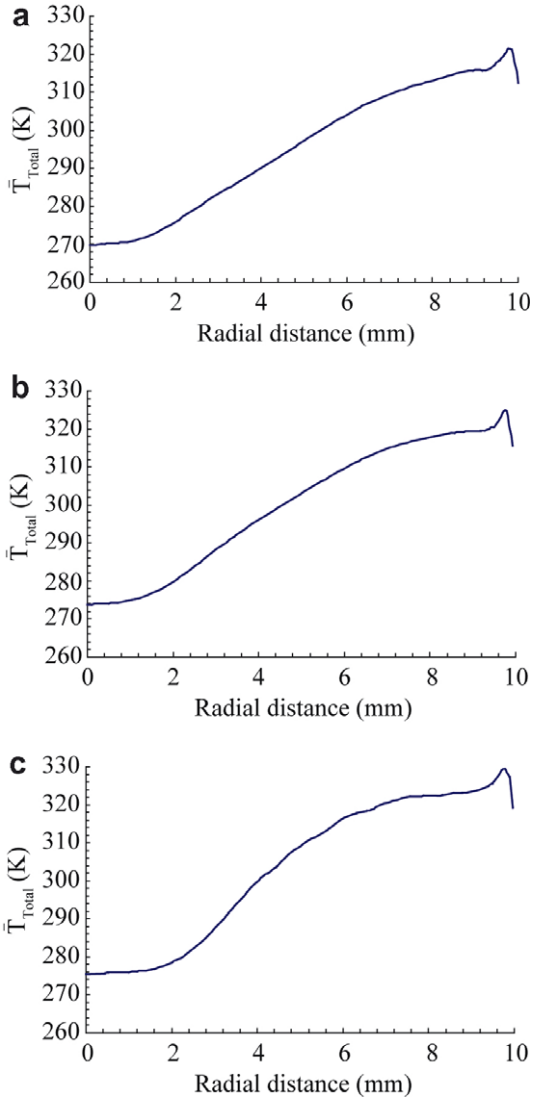

Fig. 17. Radial profiles of time averaged total temperature $\overline{T}_{total} = \frac{1}{\tau}\int_{t=t_0}^{t=t_0+\tau} T_{total}\,dt$ at: (a) $x = 50$ mm, (b) $x = 75$ mm and (c) $x = 100$ mm (Case 1). Time averaging was performed between 0.5 and 1.0 s.

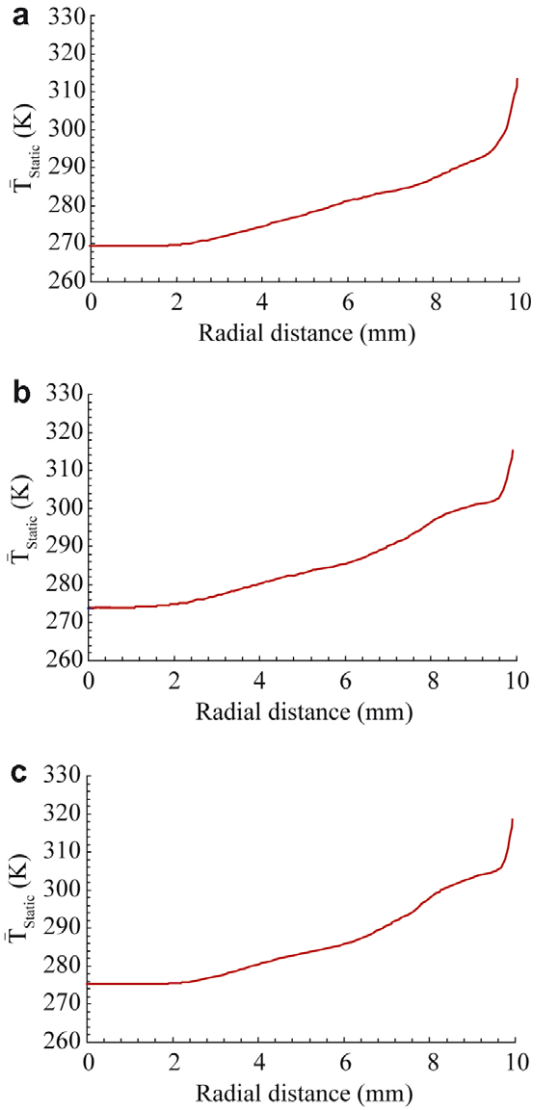

Fig. 18. Radial profiles of time averaged static temperature $\overline{T}_{static} = \frac{1}{\tau}\int_{t=t_0}^{t=t_0+\tau} T_{static}\,dt$ at: (a) $x = 50$ mm, (b) $x = 75$ mm and (c) $x = 100$ mm (Case 1). Time averaging was performed between 0.5 and 1.0 s.

the cold exit temperature separation $|\overline{T}_{in} - \overline{T}_{out,c}|$ is plotted as a function of the cold mass fraction. Unlike the results shown in Fig. 19a, $|\overline{T}_{in} - \overline{T}_{out,c}|$ shows distinct maxima where the cold mass fraction is near 0.41. This operating point for the system (maximum cooling) depends both on the geometric parameters and the inlet conditions of the incoming flow.

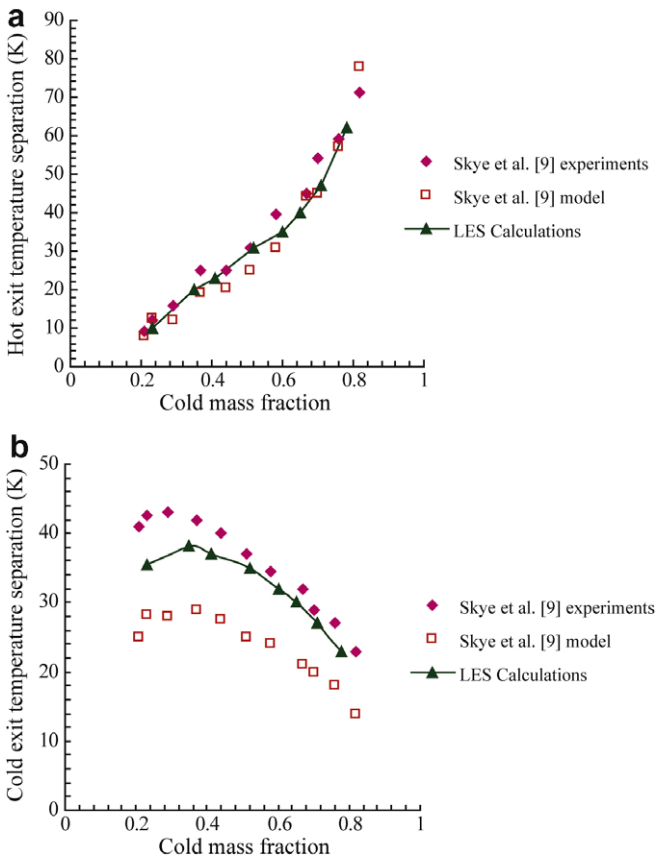

Fig. 19. (a) Hot exit temperature separation $|\overline{T}_{in} - \overline{T}_{out,h}|$ and (b) cold exit temperature separation $|\overline{T}_{in} - \overline{T}_{out,c}|$ as a function of cold mass fraction.

The temperature separation obtained from the present LES calculations were compared with the experimental and computational (k–ε model) results of Skye et al. [9] for validation. As seen in Fig. 19, the hot exit temperature separation predicted by the model is in good agreement with the experimental results. Predictions of the cold exit temperature separation is found to lie in between the experimental and computational (k–ε model) results of Skye et al. [9]. Compared to the k–ε model predictions, the hot exit temperature separation simulated by both the models were close to the experimental results. Though both the models under predicted the cold exit temperature separation, the predictions from the present LES model were found to be closer to the experimental results.

5. Conclusions

Numerical simulations of the temperature separation in a Ranque–Hilsch vortex tube were conducted. LES technique was used to model the turbulence effects. The LES methodology is based on direct solution of the large scales and sub grid scale approximation of the dynamic viscosity. Simulations were conducted for different cold mass fractions by changing the hot end pressure. The time averaged profiles indicated a hot peripheral flow and a reversing cold inner core flow together with a small secondary circulation near the cold exit. The radial velocity was found to be directed towards the tube center through most of the radial direction and towards the tube near the wall. The radial velocity profile indicated that there existed a possibility of energy separation in the radial direction. Particle traces in three-dimensional space were obtained. The particle traces indicated that the flow entering through the upper part of the inlet constitutes the cold inner core flow and the flow entering through the lower part of the inlet comprises the hot peripheral flow. The effects of cold mass fraction on the temperature separation effect were studied. The cold mass fraction was varied by varying the hot exit pressure. The hot exit temperature separation was observed to increase with an increase in the cold mass fraction. The maximum hot exit temperature separation was found for a cold mass fraction of 0.78. Apart from the cold mass fraction range of 0.23–0.41 the cold exit temperature separation was found to decrease with an increase in the cold mass fraction. The predictions from the numerical model were compared with published experimental results and k–ε model predictions. Comparing the k–ε and the LES model predictions, it was found that the temperature separations predicted by the LES model was closer to the experimental results. The model however under predicted the total temperature separation at the cold exit. Even then the general trends of the total temperature separations (hot and cold exit) predicted by the model were found to be in good in agreement with the experimental results.

References

[1] G.J. Ranque, Experiences sur la detente giratoire avec simultanes d'un echappement d'air chaud et d'un enchappement d'air froid, J. Phys. Radium 4 (7) (1933) 112–114.
[2] H.H. Bruun, Experimental investigation of energy separation in vortex tubes, J. Mech. Eng. Sci. 11 (6) (1969) 567–582.
[3] B. Ahlborn, J. Camire, J. U Keller, Low-pressure vortex tubes, J. Phys. D: Appl. Phys. 29 (1996) 1469–1472.
[4] B. Ahlborn, J.U. Keller, R. Staudt, G. Treitz, E. Rebhan, Limits of temperature separation in a vortex tube, J. Phys. D: Appl. Phys. 27 (1994) 480–488.
[5] C.M. Gao, K.J. Bosschaart, J.C.H. Zeegers, A.T.A.M. De Waele, Experimental study on a simple Ranque–Hilsch vortex tube, Cryogenics 45 (2005) 173–183.
[6] W. Frohlingsdorf, H. Unger, Numerical investigations of the compressible flow and the energy separation in the Ranque–Hilsch vortex tube, Int. J. Heat Mass Transfer 42 (1999) 415–422.
[7] U. Behera, P.J. Paul, S. Kasthurirengan, R. Karunanithi, S.N. Ram, K. Dinesh, B. Jacob, CFD analysis and experimental investigations towards optimizing the parameters of Ranque–Hilsch vortex tube, Int. J. Heat Mass Transfer 48 (2005) 1961–1973.
[8] N.F. Aljuwayhel, G.F. Nellis, S.A. Klein, Parametric and internal study of the vortex tube using a CFD model, Int. J. Refrig. 28 (2005) 442–450.
[9] H.M. Skye, G.F. Nellis, S.A. Klein, Comparison of CFD analysis to empirical data in a commercial vortex tube, Int. J. Refrig. 29 (2006) 71–80.
[10] R. Hilsch, The use of the expansion of gases in a centrifugal field as cooling processes, Rev. Sci. Instr. 18 (2) (1947) 108–113.
[11] J. Harnett, E. Eckert, Experimental study of the velocity and temperature distribution in a high velocity vortex-type flow, Trans. ASME 79 (4) (1957) 751–758.

[12] B. Ahlborn, J. Gordon, The vortex tube as a classical thermodynamic refrigeration cycle, J. Appl. Phys. 88 (6) (2000) 3645–3653.
[13] K. Stephan, S. Lin, M. Durst, F. Huang, D. Seher, An investigation of energy separation in a vortex tube, Int. J. Heat Mass Transfer 26 (3) (1983) 341–348.
[14] M. Kurosaka, Acoustic streaming in swirling flows, J. Fluid Mech. 124 (1982) 139–172.
[15] A.F. Gutsol, The Ranque effect, Physics – Uspekhi 40 (6) (1997) 639–658.
[16] J. Smagorinsky, General circulation experiments with primitive equations, I. The basic experiment, Month. Weather Rev. 91 (1963) 99–164.
[17] CFD-ACE Modules Manual V2004. Huntsville, AL: ESI US R&D, 2004.
[18] B.P. Leonard, Bounded higher-order upwind multidimensional finite-volume convection–diffusion algorithms, in: W.J. Minkowycz, E.M. Sparrow (Eds.), Advances in Numerical Heat Transfer, vol. 1, Taylor and Francis, New York, 1997, pp. 1–57.